Atomic oxygen patterning in the plasma needle biomedical source

Seán Kelly[1, a)] and Miles Turner[1]

School of Physical Science and National Centre for Plasma Science and Technology, Dublin City University, Ireland

A "plasma needle" is a cold plasma source operating at atmospheric pressure. Such sources interact strongly with living cells, but experimental studies on bacterial samples show that this interaction has a surprising pattern resulting in circular or annular killing structures. This paper presents numerical simulations showing that this pattern occurs because biologically active reactive oxygen and nitrogen species are produced dominantly where effluent from the plasma needle interacts with ambient air. A novel solution strategy is utilised coupling plasma produced neutral(uncharged) reactive species to the gas dynamics solving for steady state profiles at the treated biological surface. Numerical results are compared with experimental reports corroborating evidence for atomic oxygen as a key bactericidal species. Surface losses are considered for interaction of plasma produced reactants with reactive solid and liquid interfaces. Atomic oxygen surface reactions on a reactive solid surface with adsorption probabilities above 0.1 are shown to be limited by the flux of atomic oxygen from the plasma. Interaction of the source with an aqueous surface showed hydrogen peroxide as the dominant species at this interface.

I. INTRODUCTION

The plasma needle[1] is a cold atmospheric plasma device under study for biomedical applications[2,3,5]. The device consists of a thin tungsten wire driven by a radio frequency voltage surrounded by quartz tubing guiding helium flows of up to 2 slpm around the wire. A critical factor in its efficacy is attributed to the mixing of the helium carrier gas with air[4,10]. Mixing results in generation of reactive oxygen nitrogen species(RONS) culminating in oxidative and nitrosative stress to exposed cells. In this report we investigate numerically the role of neutral RONS species produced by the plasma needle device with a focus on the atomic oxygen and ozone patterning at the treated surface. Surface losses are discussed in this context where results of the interaction of plasma produced reactants with reactive solid and liquid interfaces are presented.

II. MODEL DESCRIPTION

A two dimensional axi-symmetric domain about the pin axis is considered, utilising the devices cylindrical symmetry (see figure 1). The dimensions are matched to experimental reports of Goree *et al*[3,4] and Sakiyama *et al.*[10] on the devices killing pattern of S. Mutans bacteria samples. A 5 mm dielectric barrier ($5\epsilon_0$) sits on a grounded plate at a distance of 3 mm below the RF driven pin. The pin diameter was taken as 0.4 mm with a taper of length 6 mm and tip diameter 0.15 mm.

In the present work, the commercial finite element partial differential equation solver COMSOL Multi-physics

————
a)Electronic mail: kellys77@mail.dcu.ie

(version 4.3a)[20] is used to find a mutually consistent solution for the reacting gas flow (which is assumed to be laminar) and the plasma discharge[6,20]. Initially, mass and momentum continuity equations (compressible Navier-Stokes) are coupled to a mass transport equation and solved in a steady state manner for a profile of the helium-air mixture. A gas temperature of 330 K is assumed with variable density and dynamic viscosity based on the mixture fraction of gaseous species. Diffusion coefficients for the neutral gas species are calculated from kinetic gas theory using the Leonard-Jones potential parameters[7]. For further information on equation formulation and boundary conditions(figure 1) see reports[7,9].

The stationary helium-air mixture profile is coupled to a self consistent fluid model of the plasma. Continuity equations for the electron density, electron energy and heavy species densities are solved with Poisson's equation for the electric field in the area NBCDIJK shown in figure 1 for CD of length 5 mm. A log substitution($N_i = ln\, n_i$) for species density n_i from the standard(linear)[8] species continuity equation is used[20]. This model is similar to that of Sakiyama *et al.*[9], who have discussed details such as boundary conditions.

Our model treats a mixture of helium and humid air (1% H_2O, 20% O_2 and 79% N_2). The reaction set is shown in table I, consisting of seven ionic species(He^+, He_2^+, N_2^+, O_2^+, O^-, O_2^- and H_2O^+) with fourteen neutral species(He, He*, He_2^*, O_2, O, $O(^1D)$, N_2, $N_2(A^3\Sigma)$, $N_2(B^3\Pi)$, N, $N(^2D)$, H_2O, OH, and H). Reactions R_{1-14} in table I follow the He-N_2 reaction scheme of Golubovski et al[22]. The oxygen reaction scheme is given by reactions R_{14-22}, nitrogen reactions by R_{23-28} and H_2O reactions by R_{29-31} in table I. A helium purity of 99.999% is used here.

The electron transport and electron impact reaction rates are preprocessed by solving the zero dimensional Boltzmann equation using the *Bolsig+ solver* software[19] with collision cross section data from the *Lx-*
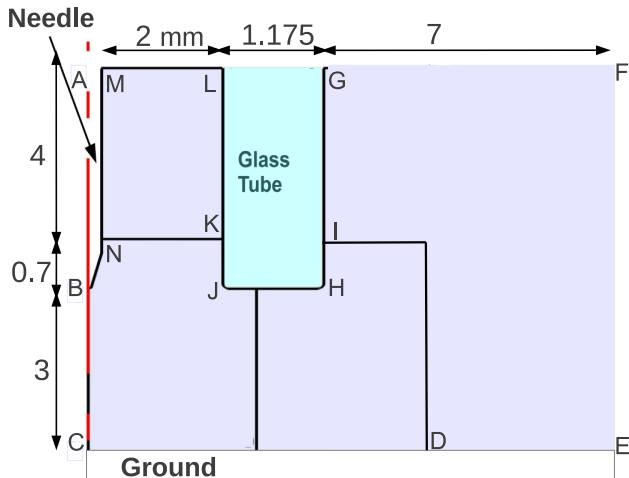
FIG. 1. Plasma needle geometry[4,9]

cat database[21] for a range of helium-air mixtures. The ion transport values are taken from literature[28] and the corresponding diffusion coefficients are calculated using the Einstein relation.

The sinusoidal applied voltage with frequency of $f = 13.56 MHz$ is given by $V_{amp}Sin(2\pi ft) + V_{dc}$ where V_{amp} is the applied voltage amplitude and V_{dc} represents the self bias voltage due to a serial blocking capacitance component in the matching circuit.

The phase averaged production rates for the neutral species formed by the plasma dynamics are coupled to a mass transport model for the reacting and convecting mixture of neutral species, which is solved over larger timescales ($t \sim 0.1$ s). These neutrals react to form ozone O_3 (see table II), various nitrogen-oxygen species N_xO_x (table III), hydrogen-oxygen species H_xO_x (table IV) and hydrogen-oxygen-nitrogen HNO_x species(table IV(R_{14-18})). The short lived reactive neutrals($N(^2D)$, $N_2(A^3\Sigma)$, $N_2(B^3\Pi)$, He^*, H and $O(^1D)$) formed during the plasma dynamics do not convect or diffuse considerably during this stage of the model.

III. RESULTS AND DISCUSSION

A. Plasma structure

The plasma model is solved for $V_{amp} = 800$ V, 900 V and 1000 V for helium inflows of 0.4, 0.5, 0.75 and 1 *slpm* until the average power deposited(P_{av}) reaches a steady state($t \sim 10$ μs) ($\delta P_{av} < 5\%$) corresponding to convergence in reactive neutral species production. The phase averaged electron density is shown in figure 2. A plasma with density $\sim 10^{20}$ m^{-3} forms around the needle tip, but this rapidly decreases to $\sim 10^{16}$ m^{-3} in the downstream region. A thin sheath structure is formed extending from the tip along the needle sides consistent with a high power mode reported for corona discharges of this type[9].

The phase averaged electron mean energy(see figure 2) displays peak values over 22 eV near the needle tip, due to the high electric field and the large curvature of the needle at this point. At the sides of the pin, electron mean energy values up to 14 eV are observed. Peak values drop in the bulk of the discharge where the mean electron energy is typically 1-2.5 eV (figure 2). These bulk values of electron energy are a key factor in providing the energy required to disassociate and excite air species, and to generate reactive neutral species.

The Helium metastable species He^* and He_2^* follow a similar spatial pattern to the plasma density with peak values of 10^{21} m^{-3} for He^*(see figure 3) and 10^{20} m^{-3} for He_2^* along the needle tip and sides. The He_2^+ ion is the dominant ionic species at the needle tip (see figure 3). This is due to the relatively small amount of impurity present in this region ($\sim$ 10 ppm). Stepwise ionisation (R_8, R_{10} in table I) and the fast charge transfer reaction between He^+ and He_2^+ result in a dominance of the He_2^+ ion around the needle tip. Away from the tip, N_2^+ becomes the dominant ionic species (figure 3) with peak values of 10^{17} m^{-3} near the central region approximately 1 mm below the pin. This is due to charge transfer reactions (R_{14} in table I) and increased penning ionisation (R_{12}, R_{13}) with increasing nitrogen in the gas mixture. The charge transfer reaction between N_2^+ and O_2^+ (R_{20} in table I) dominates the ion density in the outer radial region away from the tip (figure 3) with peak O_2^+ values of 10^{17} m^{-3} occuring approximately 2 mm below the pin and 1.5 mm from the central region. H_2O^+ ions follow a similar distribution to O_2^+ with peak values of 10^{16} m^{-3} outside the central region.

Negative ions play a dominant role in the outer regions of the discharge(see figure 4) as the fraction of O_2 in the gas mixture increases(see figure 5(right)). Peak O^- density of 10^{17} occur at air fractions in the range 10^{-3} to 10^{-2} approximately 2 mm from the centre. An increasing O_2 fraction outside the central region leads to the dominance of O_2^-(see figure 4 and reaction R_{33} in table I). Negative ions are the dominant negative charge carrier as the air fraction increases in the range 10^{-2} to 10^{-1}. This eventually leads to a large decrease in the plasma density in the outer regions of the discharge as power is increasingly coupled to negative ions over electrons.

B. Reactive neutrals

The neutral oxygen species produced by the plasma include atomic oxygen O, excited species $O(^1D)$ and the long lived molecular oxygen metastable $O_2(a^1\Delta)$. The phase averaged atomic oxygen production rate is shown in figure 5 with corresponding air fraction (right) for a
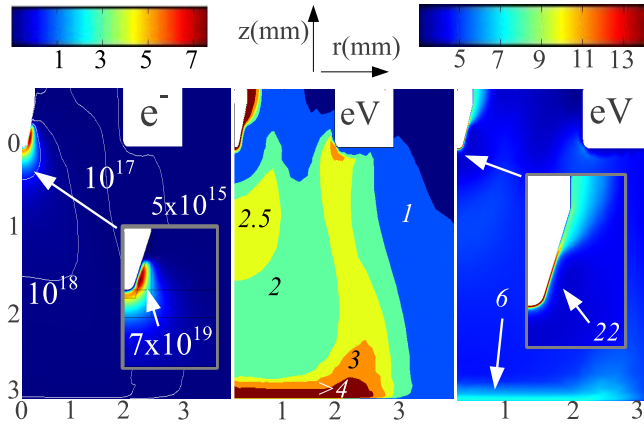
FIG. 2. Electron(left) phase averaged density m^{-3}, electron energy(filled contour 1-4eV(middle)) and electron energy(right): 0.5 slpm, V$_{applied}$ = 900 V, V$_{dc}$ = 0 V

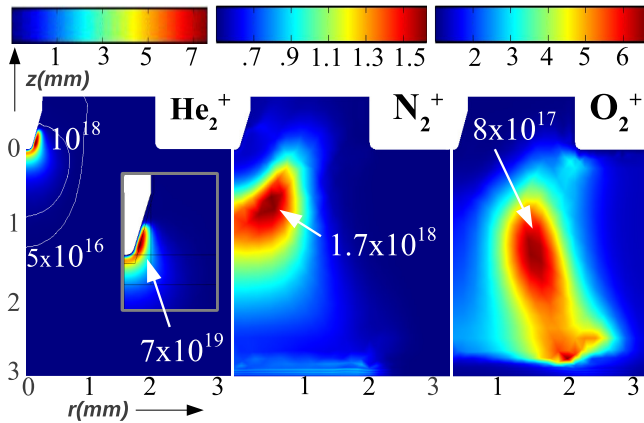FIG. 3. He$_2^+$(left), N$_2^+$(middle) and O$_2^+$(right) phase averaged density m^{-3}: 0.5 slpm, V$_{applied}$ = 900 V, V$_{dc}$ = 0 V

FIG. 4. O$^-$(left), O$_2^-$(middle) and He*(right) phase averaged density m^{-3}: 0.5 slpm, V$_{applied}$ = 900 V, V$_{dc}$ = 0 V

FIG. 5. O(left), N(middle) phase averaged production rate m^{-3}s^{-1} & air mixture fraction: 0.5 slpm, V$_{applied}$ = 900 V

flow rate of 0.5 slpm. The spatial peak production of atomic oxygen occurs in the region where the air fraction is of the order 10^{-2} and the plasma density is of the order of 10^{17} m^{-3} (figure 2). Values of 1.1×10^{25} m^{-3}s are observed in the region of 10^{-3} - 10^{-2} air fraction. Three factors determine the patterning seen here: the interaction of plasma (electron) density, electron energy and the available oxygen density (air fraction). Atomic oxygen is produced via dissociation, due to electron impact by reactions R$_{16}$ and R$_{17}$ with threshold energies of 5.58 eV and 8.4 eV and also by dissociative recombination reaction R$_{18}$ in table I. R$_{17}$ was found to be the dominant reaction producing atomic oxygen. The production rate of O(^1D) follows a similar pattern to the atomic oxygen production consistent with reaction R$_{17}$ in table I. O$_2$($a^1\Delta$) displays a more diffuse pattern of production in comparison to O and O(^1D) due to its low excitation energy threshold of 0.98 eV. O$_2$($a^1\Delta$) peak production of 5×10^{24} m^{-3} s^{-1} are observed in the region of 10^{-2} air fraction.
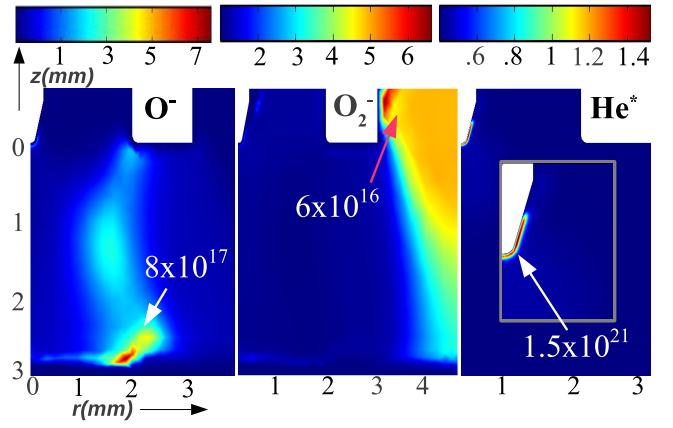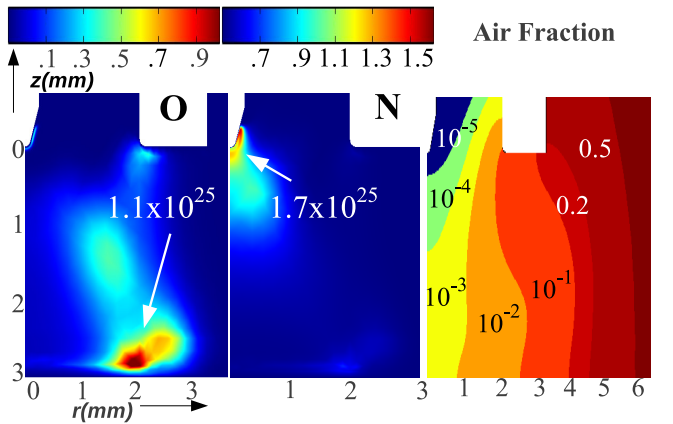
The phase averaged N production rates are shown in figure 5. Formation of N is by direct dissociation of N$_2$(R$_{26}$ table I) and disociative recombination of N$_2^+$(R$_{28}$ table I). The latter reaction proves dominant in the area around the needle tip where N$_2^+$ ion densities are large. The production rate of N(^2D) follows a similar pattern to the atomic nitrogen production consistent with the chemistry used(R$_{27}$, R$_{28}$ in table I). The phase averaged N$_2$($A^3\Sigma$) and N$_2$($B^3\Pi$) spatial production patterns show similar behaviour to O$_2$($a^1\Delta$) production with peak values of $3.6 - 5 \times 10^{25}$ m^{-3} s^{-1} observed.

OH and H are formed via the direct dissociation and dissociative recombination of H$_2$O and H$_2$O$^+$(R$_{29-31}$ table I) and show a similar production pattern as O. Peak values of 9×10^{22} m^{-3} s^{-1} are found.

C. Reactive species at surface

The steady state oxygen and ozone distribution on the grounded surface is shown in figure 6 for 0.4, 0.5, 0.75 and 1 slpm inlet flows at 900 V. Peak O and O$_3$ values shift
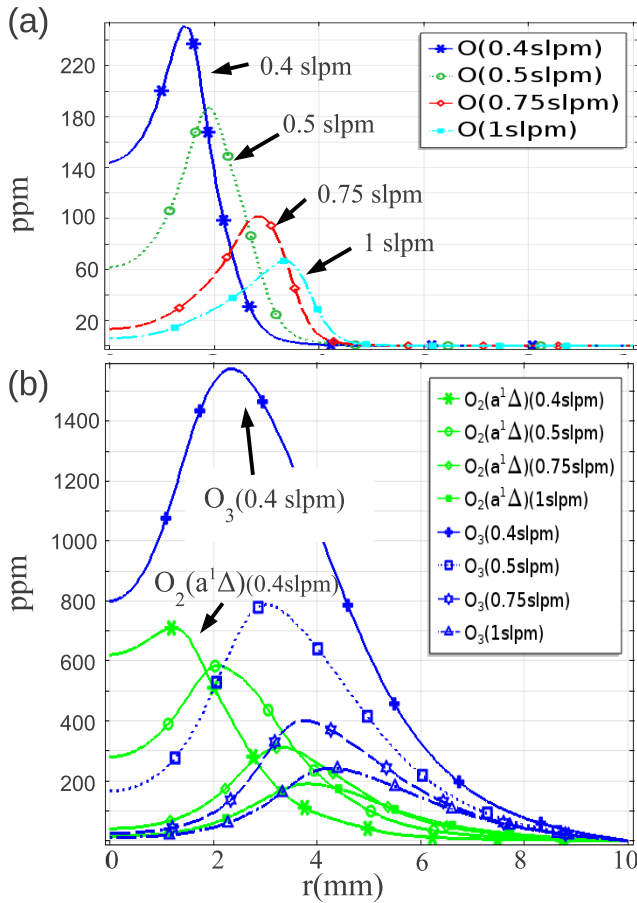
FIG. 6. O (a) & O_3, $O_2(a^1\Delta)$(b) on surface(ppm): 0.4 slpm, 0.5 slpm, 0.75 slpm & 1 slpm. $V_{applied} = 900$ V

FIG. 7. Reactive Oxygen Nitrogen Species(RONS) density at surface(ppm): 0.4 slpm, $V_{applied} = 900$ V

4 ppm peaking in the central region.

Figure 7(right) shows the steady state density for hydrogen-oxygen-nitrogen species. Peak values of 12 ppm hydrogen peroxide H_2O_2 and 8.5 ppm of hydroperoxyl radical HO_2 were found at the treatment surface with maximum values occurring within 5 mm of the centre. Nitrous acid HNO_2 and nitric acid HNO_3 values of less than 5 ppm are shown in figure 7(right).

D. Experimental comparison

In this section a comparison of our model results from optical diagnostics on a plasma needle treated surface by Sakiyama et al.[10] is discussed. Sakiyama's report presents atomic oxygen density values on a treated surface corroborating earlier studies by Goree et al[3,4] on circular and annular killing patterns observed on plasma needle treated *S. Mutans* bacterial samples. The grounded surface used by Sakiyama in this report is a quartz cuvette(SiO$_2$) which is a largely *inactive surface* to oxidation by the plasma produced RONS(O, O_3, $O_2(a^1\Delta)$, ..). This allows direct comparison with results discussed in section III C for an inactive solid treatment surface(boundary CE in figure 1). Figure 8 shows atomic oxygen density at inlet flows of 0.4 slpm and 1 splm for a range of applied voltages. Peak values at 0.5 slpm as reported by Sakiyama et al. show an atomic oxygen density peak of 5×10^{21} m^{-3} within 2 mm of the centre. This is in good agreement with similar peak values for 0.4 slpm at 900-1000 V shown in figure 8. At 1 slpm inlet flows Sakiyama reports a peak in the atomic oxygen at 3 mm outside the central region with density of 4×10^{21} m^{-3}. Figure 8 shows a similar density peaking at 3 mm but with lower peak values of 2×10^{21} m^{-3}. Such a divergence of results is possibly due to unmatched power conditions used experimentally(applied voltage conditions not reported) or the DC bias voltage which is not accounted for in this numerical study.

outwards in tandem (separated by approximately 1 mm) as the available air fraction decreases in the central region at higher flows. The decrease in the peak magnitude is due to the lower plasma density and electron energy available outside the central region. At flows of 0.4 slpm peak oxygen values of over 250 ppm(5.5×10^{21} m^{-3}) occur within 2 mm of the centre.

The balance between the competitive reactions in table II determine the *atomic oxygen-ozone balance* in the region below the pin. Ozone generation is dominated by reaction with Helium in the central region and N_2, O_2 outside the central region(R_2 in table II). Quenching of ozone is due to reactions with hydrogen-oxygen radicals(OH, H, HO_2)($R_{5,14,24}$ in table IV) and nitrogen-oxides (NO, NO_2)($R_{17,18}$ in table III) but is dominated by quenching by $O_2(a^1\Delta)$ (R_{11} in table II) with rate values of the order of 10^{23} m^{-3} s^{-1} across the domain.

The steady state distribution of nitrogen-oxygen species is shown in figure 7 for an inlet flow of 0.4 slpm and applied voltage of 900 V. Atomic nitrogen was found in the central region in excess of 17 ppm. Nitrous oxide N_2O was found to be the dominant nitrogen-oxygen species with peak values in the central region of 40 ppm. Values of NO and NO_2 found were less than 13 ppm and
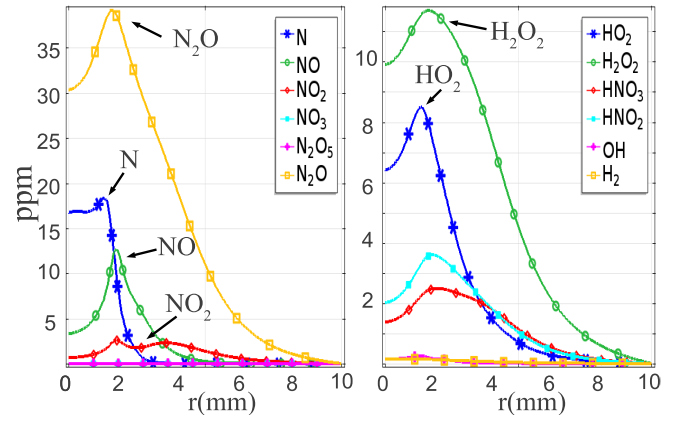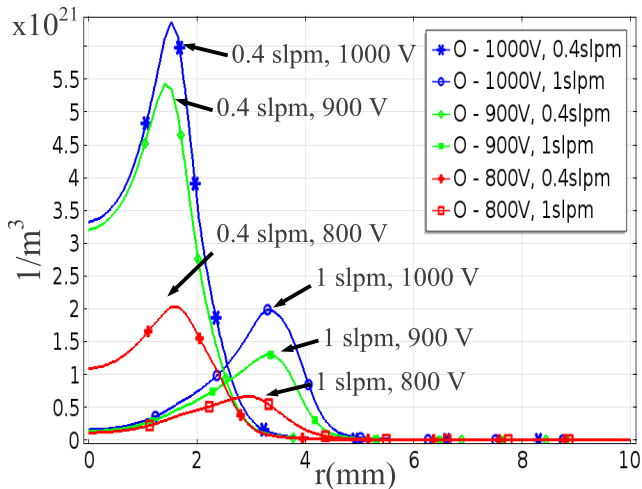
FIG. 8. Atomic oxygen density at surface(m^{-3}): 0.4 slpm and 1 slpm for $V_{applied} = 800, 900, 1000$ V
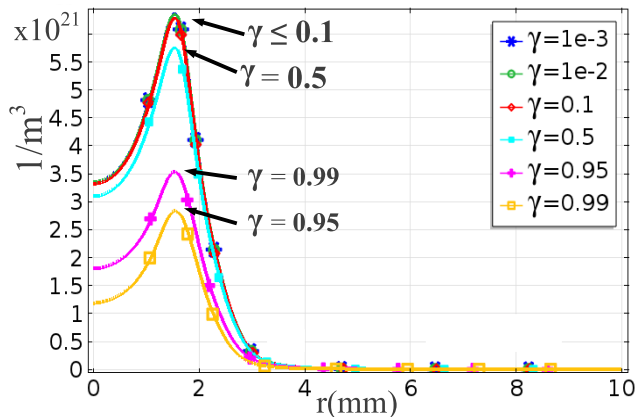

FIG. 9. Atomic oxygen density at a reactive solid surface(m^{-3}) for a range of adsorption probabilities(γ): 0.4 slpm, $V_{applied} = 1000$ V

E. Surface interaction

The interaction of plasma produced RONS with *active surfaces* is highly dependent on the surface properties of the material being treated. Atmospheric pressure plasmas have been shown to increase the surface energy(wetability) of various solid surfaces of hydrocarbon polymers such as perspex or polystyrene[40], to kill bacteria, promote wound healing in mammalian cells and kill cancerous cells[36–38]. These applications occur in both aqueous and dry environments adding to the complexity of interaction. In this section we discuss the interaction of the plasma needle with *reactive* solid and aqueous boundaries in the context of the results presented above.

1. Solid surface interaction

Adsorption of plasma produced RONS on a *dry* solid surface of a non-biological or biological polymer initially causes radical formation which propagates a chain reaction of radical production on the surface. Initial radical formation breaks C-H, C-O and C-C bonds on the polymer surface such as peptidoglycan in bacteria cell walls[41], lipid layers in animal cell membranes[42] or plastic materials such as polypropolene[27]. RONS flux loss at a treated surface is primarily dependent on the density of available reaction sites and the reaction rate for each species adsorption. The initiated radical formation on a treated surface is followed by a sequence of radical reactions(propagation) and eventual radical termination often producing a sequence of gaseous by-products which may interact with plasma RONS at the interface. A full model of this interaction for various surfaces is beyond the scope of this report.

Here we investigate surfaces losses at a reactive treatment surface by considering a simplified model of flux loss for a variety of adsorption probability values(γ) where $(1 > \gamma > 0)$ for each species[39]. The flux loss at the treated boundary(CE in figure 1) is given by the product $\gamma_i \Gamma_{surf,i}$ where $\Gamma_{surf,i}$ is the normal component of the surface flux for species i. Our reacting gas model is solved using the same flux loss probability γ for O, O_3 and $O_2(a^1\Delta)$ reactive oxygen species[39]. Steady state results for the atomic oxygen density at the treated surface for various reaction probabilities γ are shown in figure 9. We see that for values of $\gamma > 0.1$ species density at the surface(central region) begin to drop significantly. Figure 9 shows that atomic oxygen surface reactions with reaction/adsorption probabilities $\gamma > 0.1$ will be limited significantly by the atomic oxygen flux from the plasma. Reaction probabilities for atomic oxygen interacting with polypropylene surfaces[27] have been estimated as typically < 0.01 while reaction probabilities on biological polymers such as lipid layers of cell membranes are not yet fully understood.

2. Water surface interaction

Many application environments such as treatment of living tissues involve biological targets covered in a liquid layer predominately constituent of water. In this scenario the plasma produced RONS are effected remarkable by interaction with a H_2O liquid layer. The gas mixture at the liquid interface is saturated with water vapour which reacts with plasma produced RONS. To estimate this water vapour density we consider the *Antoine equation* allowing the calculation of the (saturated) partial pressure of the water vapour in the gas mixture at the interface[44]. Assuming a temperature of 293.15 K the partial pressure of H_2O vapour was calculated as 0.023 fraction of the total atmosphere[43]. The average gas density at the surface(boundary CE) for an inlet flow of 0.4 slpm is 2.2 $\times 10^{25}$
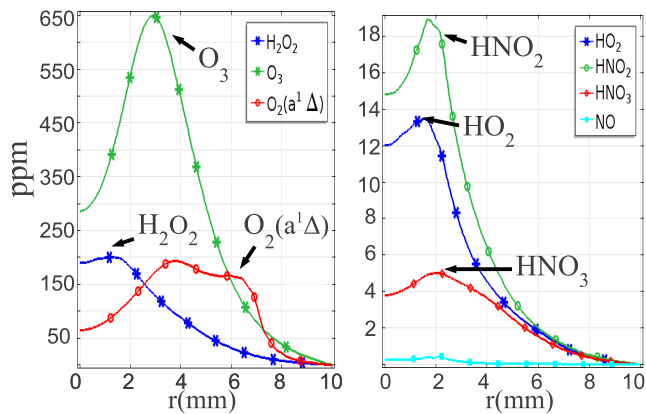
FIG. 10. Reactive Oxygen Nitrogen Species(RONS) density at water surface(ppm): 0.4 slpm, $V_{applied} = 1000$ V

m^{-3} giving an average H_2O gas density of 5×10^{23} m^{-3} at the interface. We consider the effects of interaction with this vapour layer on RONS species by including an additional reaction chemistry at the surface CE in our model. An additional chemistry shown in table V is considered on the boundary CE with a H_2O density 0.023 fraction of the total gas density across the boundary.

Results shown in figure 10 represent the non-equilibrium(undissolved) gaseous species density at the water surface for 1000 V applied voltage at an inlet flow of 0.4 slpm. Atomic oxygen reacts strongly with the H_2O vapour layer to form $OH(R_1$ in table V) which further reacts with H_2O to form hydrogen peroxide $H_2O_2(R_{11}$ in table V). Reaction of O_3 with the vapour layer results in further O formation. Comparison of O_3 values on an inactive surface show a 50% drop in O_3 density over an aqueous surface. This atomic oxygen production due to O_3 reaction with water is responsible for a more diffuse H_2O_2 pattern on the treated surface when compared with the O spatial pattern over a solid surface. Peak values of H_2O_2 of 200 ppm in the central region are shown in figure 10(left) falling to 50 ppm at 5 mm from the centre. $O_2(a^1\Delta)$ is quenched considerably to O_2 when it interacts with the H_2O vapour layer(R_4 in table V). Comparison of $O_2(a^1\Delta)$ values on an inactive surface show a ~600% drop in density in the central region over an aqueous surface. At 4 mm from the center however $O_2(a^1\Delta)$ actually increases by approximately 100-200% due to the decrease in O_3 before tending to zero beyond 9 mm.

Equilibrium occurs due to dissolution of gaseous species into the water volume which is assumed to proceed reaction at the interface. Henry's law constants shown in table VI represent the concentration ratio of dissolved and undissolved gases once equilibria is reached. If we assume that the total available species($n_{total} = n_{gas} + n_{aqueos}$) for dissolution is equal to the non-equilibrium distributions shown in figure the fraction of dissolved and undissolved species in equilibria is given by the ratios $1/(1+K_H^{cc})$ and $1/(1+1/K_H^{cc})$ respectively shown in table VI. Table VI clearly shows that H_2O_2, HNO_2,

HO_2 and HNO_3(see figure 10(right)) with solubilities of 99.99%, 67%, 99.6% and 99.99% respectively (given by $1/(1+1/K_H^{cc})$) are the most important species for treatment of aqueous surfaces.

IV. CONCLUSION

In this paper the behaviour of neutral reactive species of the "plasma needle" source is investigated. Peak production of atomic oxygen due to interaction of the plasma with air species occurred at regions of air fraction from 10^{-3} to 10^{-2}. Increasing the gas flow shifted the peak atomic oxygen at the surface from the central to the outer discharge regions correlating to solid circular and annular type atomic oxygen distributions previously reported[4,10]. Peak atomic oxygen density of 10^{21} and ozone density of 10^{22} m^{-3} were presented here.

Surface loss studies revealed that atomic oxygen surface reactions on a reactive solid surface with adsorption probabilities greater than 0.1 are limited by the flux of atomic oxygen from the plasma. Interaction of the source with an aqueous surface showed hydrogen peroxide as the dominant species at this interface with significant hydroperoxyl radical, nitrous acid and nitric acid densities also present.

Appendix A: Chemistry tables

Ref[a]	Reaction	Rate[b]
R_1^{19}	e+He→He+e	$BOLSIG+$
R_2^{19}	e+He→He*+e	$BOLSIG+$
R_3^{19}	e+He→2e + He$^+$	$BOLSIG+$
R_4^{29}	e+He* →e+He	2.9×10^{-15}
R_5^{22}	e+He$_2^+$ →He*+He	$8.9 \times 10^{-15}(T_g/T_e)^{1.5}$
R_6^{22}	He$^+$+2He→He+He$_2^+$	1.1×10^{-43}
R_7^{22}	He*+2He→He+He$_2^*$	2×10^{-46}
R_8^{22}	He*+He* →e+He$_2^+$	1.5×10^{-15}
R_9^{22}	He$_2^*$ → 2He	10^4
R_{10}^{22}	He$_2^*$+He$_2^*$ →e+He$_2^+$+2He	1.5×10^{-15}
R_{11}^{22}	e+N$_2^+$ →2N	$4.8 \times 10^{-13}(T_g/T_e)^{0.5}$
R_{12}^{22}	He*+N$_2$ →He+N$_2^+$+e	5×10^{-17}
R_{13}^{22}	He$_2^*$+N$_2$ →2He+N$_2^+$+e	3×10^{-17}
R_{14}^{22}	He$_2^+$+N$_2$ →He*+N$_2^+$	1.4×10^{-15}
R_{15}^{19}	e+O$_2$ →2e + O$_2^+$	$BOLSIG+$
R_{16}^{19}	e+O$_2$ →e+2O	$BOLSIG+$
R_{17}^{19}	e+O$_2$ →e+O+O(^{1}D)	$BOLSIG+$
R_{18}^{23}	e+O$_2^+$ →2O	$6 \times 10^{-11}T_e^{-1}$
R_{19}^{19}	e+O$_2$ →e+O$_2(a^1\Delta)$	$BOLSIG+$
R_{20}^{23}	N$_2^+$+O$_2$ →N$_2$+O$_2^+$	$1.04 \times 10^{-15}T_g^{-0.5}$
R_{21}^{16}	He*+O$_2$ →He+O$_2^+$+e	$2.54 \times 10^{-16}(T_g/300)^{0.5}$
R_{22}^{24}	He$_2^*$+O$_2$ →2He+O$_2^+$+e	$1 \times 10^{-16}(T_g/300)^{0.5}$
R_{23}^{19}	e+N$_2$ →e+N$_2(A^3\Sigma)$	$BOLSIG+$
R_{24}^{19}	e+N$_2$ → e+N$_2(B^3\Pi)$	$BOLSIG+$
R_{25}^{19}	N$_2(B^3\Pi)$→N$_2(A^3\Sigma)$	1.2×10^5
R_{26}^{19}	e+N$_2$ →e+N(^2D)+N	$BOLSIG+$
R_{27}^{19}	e+N→e+N(^2D)	$BOLSIG+$
R_{28}^{23}	e+N$_2^+$ →N(^2D)+N	$1.5 \times 10^{-12}/T_e^{0.7}$
R_{29}^{19}	e+ H$_2$O→2e + H$_2$O$^+$	$BOLSIG+$
R_{30}^{13}	e+H$_2$O$^+$ →OH+H	$2.73 \times 10^{-12}T_g^{-0.5}$
R_{31}^{19}	e+H$_2$O→e+OH+H	$BOLSIG+$
R_{32}^{19}	e+O$_2$ → O+O$^-$	$BOLSIG+$
R_{33}^{23}	e+2O$_2$ → O$_2^-$ + O$_2$	$6 \times 10^{-39}T_e^{-1}$
R_{34}^{23}	O$^-$ + O$_2^+$ → O + O$_2$	$3.464 \times 10^{-12}T_g^{-0.5}$
R_{35}^{23}	O$_2^-$ + O$_2^+$ + M^c → 2O$_2$ + M	$3.12 \times 10^{-31}T_g^{-2.5}$

[a] superscript n indicates reference for ith reaction R$_i^n$
[b] Rates in units $[m^3/s]$, $[m^6/s]$(3 body reactions), T$_g$(K) gas temperature, T$_e$(K) electron temperature
[c] M represents background gases He, N$_2$, O$_2$

TABLE I. Plasma chemistry

Ref[a]	Reaction	Rate Coefficient[b]
R_1^{12}	O+O+M^c→O$_2$+M	$2.15 \times 10^{-46}\exp(345/T_g)$
R_2^{12}	O+O$_2$+M→O$_3$+M	$6.9 \times 10^{-46}(300/T_g)^{1.25}$
R_3^{12}	O+O$_2$+O→O$_3$+O	$2.15 \times 10^{-46}\exp(345/T_g)$
R_4^{12}	O+O$_2$+O$_3$ →2O$_3$	$4.6 \times 10^{-47}\exp(1050/T_g)$
R_5^{12}	O+O$_3$ →2O$_2$	$1.8 \times 10^{-17}\exp(-2300/T_g)$
R_6^{13}	O+O(^{1}D) →2O	8×10^{-18}
R_7^{16}	O(^{1}D)+M →O+M	1×10^{-19}
R_8^{13}	O(^{1}D)+O$_3$ →2O+O$_2$	1.2×10^{-16}
R_9^{15}	O(^{1}D)+O$_2(a^1\Delta)$→O+O$_2$	1.0×10^{-17}
R_{10}^{13}	O(^{1}D)+O$_2$ →O+O$_2(a^1\Delta)$	1.0×10^{-18}
R_{11}^{14}	O$_2(a^1\Delta)$+O$_3$ →O+2O$_2$	$5.2 \times 10^{-17}\exp(-2840/T_g)$
R_{12}^{17}	O$_2(a^1\Delta)$+M → O$_2$+M	2.01×10^{-26}
R_{13}^{16}	O$_3$+M → O+O$_2$+M	$1.56 \times 10^{-15}\exp(-11490/T_g)$
R_{14}^{12}	O$_3$+O$_3$ →O+O$_2$+O$_3$	$1.65 \times 10^{-15}\exp(-11400/T_g)$

[a] superscript n indicates reference for ith reaction R$_i^n$
[b] Rates in units $[m^3/s]$, $[m^6/s]$(3 body reactions), T$_g$(K) gas temperature, T$_e$(K) electron temperature
[c] M represents background gases He, N$_2$, O$_2$

TABLE II. Oxygen chemistry

Ref[a]	Reaction	Rate Coefficient[b]
R_1^{14}	N+O+M^c→NO+M	$6.3 \times 10^{-45}\exp(140/T_g)$
R_2^{13}	N+N+M→N$_2$+M	$8.3 \times 10^{-46}\exp(500/T_g)$
R_3^{14}	N+O$_2$ →NO+O	$1.5 \times 10^{-17}\exp(-3600/T_g)$
R_4^{14}	N+NO→N$_2$+O$_2$	$2.1 \times 10^{-17}\exp(100/T_g)$
R_5^{13}	N+NO$_2$ →N$_2$O+O	$5.8 \times 10^{-18}\exp(220/T_g)$
R_6^{14}	N+OH→H+NO	7.5×10^{-17}
R_7^{14}	N(^{2}D)+M →N+M	$5 \times 10^{-18}\exp(-1620/T_g)$
R_8^{23}	N(^{2}D)+O$_2$ →NO+O(^{1}D)	$6 \times 10^{-18}(T_g/300)^{0.5}$
R_9^{23}	N(^{2}D)+NO→N$_2$O	6×10^{-17}
R_{10}^{23}	N(^{2}D)+NO→N$_2$+O	4.5×10^{-17}
R_{11}^{14}	N$_2(A^3\Sigma)$+M→N$_2$+M	2.2×10^{-20}
R_{12}^{23}	N$_2(A^3\Sigma)$+O→NO+N(^{2}D)	7×10^{-18}
R_{13}^{23}	N$_2(A^3\Sigma)$+O$_2$ →N$_2$+2O	2.54×10^{-18}
R_{14}^{23}	N$_2(A^3\Sigma)$+N$_2$O→ N$_2$+N+NO	1×10^{-17}
R_{15}^{14}	N$_2(A^3\Sigma)$+NO$_2$ → N$_2$+NO+O	1.3×10^{-17}
R_{16}^{14}	NO+O+M→NO$_2$+M	$1 \times 10^{-43}(300/T_g)^{1.6}$
R_{17}^{14}	NO+O$_3$ →NO$_2$+O$_2$	$1.8 \times 10^{-18}\exp(-1370/T_g)$
R_{18}^{14}	NO$_2$+O$_3$ →NO$_3$+O$_2$	$1.4 \times 10^{-19}\exp(-2470/T_g)$
R_{19}^{17}	NO$_2$+NO$_3$+M→N$_2$O$_5$+M	$2.8 \times 10^{-42}(300/T_g)^{3.5}$
R_{20}^{14}	NO$_2$+O→NO+O$_2$	$6.5 \times 10^{-18}\exp(120/T_g)$
R_{21}^{14}	NO$_2$+O(^{1}D)→NO+O$_2$	1.4×10^{-16}
R_{22}^{17}	N$_2$+O(^{1}D)+M→N$_2$O+M	9×10^{-49}
R_{23}^{14}	N$_2$O+O(^{1}D)→NO+NO	1.4×10^{-16}
R_{24}^{14}	NO$_3$+O→NO$_2$+O$_2$	1.7×10^{-17}
R_{25}^{17}	N$_2$O$_5$+M→NO$_2$+NO$_3$+M	$((300 \times 10^{-9})/T_g)^{3.5}$ $\times \exp(-11000/T_g)$

[a] superscript n indicates reference for ith reaction R$_i^n$
[b] Rates in units $[m^3/s]$, $[m^6/s]$(3 body reactions), T$_g$(K) gas temperature, T$_e$(K) electron temperature
[c] M represents background gases He, N$_2$, O$_2$

TABLE III. Nitrogen-oxygen chemistry

Ref[a]	Reaction	Rate Coefficient[b]
R_1[31]	$H+H+M$[c]$\rightarrow H_2+M$	$1.8 \times 10^{-42}/T_g$
R_2[27]	$H+O+M\rightarrow OH+M$	1.62×10^{-44}
R_3[17]	$H+O_2+M\rightarrow HO_2+M$	$5.4 \times 10^{-44}(T_g/300)^{-1.8}$
R_4[31]	$H+OH+M\rightarrow H_2O+M$	$6.1 \times 10^{-38}/T_g^2)$
R_5[13]	$H+O_3 \rightarrow OH+O_2$	$2.8 \times 10^{-17}(T_g/300)^{0.75}$
R_6[17]	$H+HO_2 \rightarrow H_2+O_2$	5.6×10^{-18}
R_7[17]	$H+HO_2 \rightarrow H_2O+O$	2.4×10^{-18}
R_8[32]	$H+H_2O_2 \rightarrow OH+H_2O$	1.69×10^{-17} exp(-1800/T_g)
R_9[13]	$H+NO_2 \rightarrow OH+NO$	1.47×10^{-16}
R_{10}[13]	$H+NO_3 \rightarrow OH+NO_2$	5.8×10^{-16} exp(750/T_g)
R_{11}[13]	$H+HNO_2 \rightarrow H_2+NO_2$	2×10^{-17} exp(-3700/T_g)
R_{12}[33]	$H+HNO_3 \rightarrow H_2O+NO_2$	$1.39 \times 10^{-20}(T_g/298)^{3.29}$
		$\times$ exp(-3160/T_g)
R_{13}[13]	$OH+O\rightarrow H+O_2$	2.2×10^{-17} exp(-350/T_g)
R_{14}[13]	$OH+O_3 \rightarrow HO_2+O_2$	1.6×10^{-18} exp(-1000/T_g)
R_{15}[27]	$OH+OH+M\rightarrow H_2O_2+M$	$6.9 \times 10^{-43}(T_g/300)^{-0.8}$
R_{16}[13]	$OH+OH\rightarrow O+H_2O$	8.8×10^{-18} exp(-503/T_g)
R_{17}[13]	$OH+H_2 \rightarrow H+H_2O$	3.2×10^{-17} exp(-2600/T_g)
R_{18}[17]	$OH+H_2O_2 \rightarrow HO_2+H_2O$	2.9×10^{-18} exp(-160/T_g)
R_{19}[14]	$OH+NO+M\rightarrow HNO_2+M$	$7.4 \times 10^{-43}(300/T_g)^{2.4}$
R_{20}[14]	$OH+NO_2+M\rightarrow HNO_3+M$	$2.2 \times 10^{-42}(300/T_g)^{2.9}$
R_{21}[17]	$OH+NO_3 \rightarrow HO_2+NO_2$	2×10^{-17}
R_{22}[27]	$OH+HNO_2 \rightarrow NO_2+H_2O$	$1.8 \times 10^{-17}(-390/T_g)$
R_{23}[14]	$OH+HNO_3 \rightarrow NO_3+H_2O$	1.5×10^{-20} exp(650/T_g)
R_{24}[17]	$HO_2+O_3 \rightarrow OH+2O_2$	1.4×10^{-20} exp(-600/T_g)
R_{25}[17]	$HO_2+HO_2 \rightarrow H_2O_2+O_2$	2.2×10^{-19} exp(600/T_g)
R_{26}[30]	$HNO_2+HNO_3 \rightarrow 2NO_2+H_2O$	1.6×10^{-23}

[a] superscript n indicates reference for i^{th} reaction R_i^n
[b] Rates in units $[m^3/s]$, $[m^6/s]$(3 body reactions), T_g(K) gas
  temperature, T_e(K) electron temperature
[c] M represents background gases He, N_2, O_2

TABLE IV. Hydrogen-nitrogen-oxygen chemistry

Species	K_H^{cc}	$1/(1+K_H^{cc})$	$1/(1+1/K_H^{cc})$
He	1.514e-5	0.99999	1e-5
O_2	5.32e-4	0.9995	5e-4
N_2	2.66e-5	0.99997	3e-5
O_3	4.91e-5	0.99995	5e-5
NO	7.77e-5	0.99992	8e-5
NO_2	1.68e-3	0.998	2e-3
N_2O	1.02e-3	0.999	1e-3
NO_3	7.37e-2	0.93	7e-2
N_2O_5	8.59e-2	0.92	0.08
H_2	3.19e-5	0.99997	3e-5
OH	1.19	0.457	0.543
HO_2	233	4e-3	0.996
H_2O_2	2905	3e-4	0.9997
HNO_2	2.01	0.33	0.67
HNO_3	8593	1e-4	0.9999

TABLE VI. Henry's law constant(solubilities) in water at T=298.15K[34]

Ref[a]	Reaction	Rate Coefficient[b]
R_1[12]	$O+H_2O\rightarrow 2OH+O_2$	1.0×10^{-17} exp(-550/T_g)
R_2[12]	$O+O+H_2O\rightarrow O_2+H_2O$	2.15×10^{-46} exp(345/T_g)
R_3[12]	$O+O_2+H_2O\rightarrow O_3+H_2O$	$6.9 \times 10^{-46}(300/T_g)^{1.25}$
R_4[43]	$O_2(a^1\Delta)+H_2O\rightarrow O_2+H_2O$	3×10^{-24}
R_5[16]	$O_3+H_2O\rightarrow O+O_2+H_2O$	1.56×10^{-15}exp(-11490/T_g)
R_6[14]	$N+O+H_2O\rightarrow NO+H_2O$	6.3×10^{-45} exp(140/T_g)
R_7[13]	$N+N+H_2O\rightarrow N_2+H_2O$	8.3×10^{-46} exp(500/T_g)
R_8[14]	$NO+O+H_2O\rightarrow NO_2+H_2O$	$1 \times 10^{-43}(300/T_g)^{1.6}$
R_9[17]	$NO_2+NO_3+H_2O\rightarrow N_2O_5+H_2O$	$2.8 \times 10^{-42}(300/T_g)^{3.5}$
R_{10}[17]	$N_2O_5+H_2O\rightarrow NO_2+NO_3+H_2O$	$((300 \times 10^{-9})/T_g)^{3.5}$
R_{11}[27]	$OH+OH+H_2O\rightarrow H_2O_2+H_2O$	$6.9 \times 10^{-43}(T_g/300)^{-0.8}$
		$\times$ exp(-11000/T_g)
R_{19}[14]	$OH+NO+H_2O\rightarrow HNO_2+H_2O$	$7.4 \times 10^{-43}(300/T_g)^{2.4}$
R_{20}[14]	$OH+NO_2+H_2O\rightarrow HNO_3+H_2O$	$2.2 \times 10^{-42}(300/T_g)^{2.9}$

[a] superscript n indicates reference for i^{th} reaction R_i^n
[b] Rates in units $[m^3/s]$, $[m^6/s]$(3 body reactions), T_g(K) gas
  temperature, T_e(K) electron temperature

TABLE V. Surface H_2O chemistry

[1] *E Stoffels, A J Flikweert, W W Stoffels, G M W Kroesen, Plasma Sources Sci. Technol., 11, 2002*

[2] *E Stoffels, I E Kieft, R E J Sladek, L J M van den Bedem, E P van der Laan, M Steinbuch, Plasma Sources Sci. Technol., 15, 2006*

[3] *J. Goree, Liu B., Drake D., Stoffels E., IEEE Trans. Plasma Sci., 34, 2006*

[4] *J. Goree, Liu B. and Drake D., IEEE Trans. Plasma Sci., 39, 2006*

[5] *G Y Park, S J Parkm, M Y Choi, I G Koo, J H Byun, J W Hong, J Y Sim, G J Collins and J K Lee, Plasma Sources Sci. Technol., 21, 2012*

[6] *I. Rafatov, E. A. Bogdanov & A. A. Kudryavtsev, Phys. Plasmas, 19, 2012*

[7] *B. B. Bird, W. E. Stewart and E. N. Lightfoot, Transport phenomena, Wiley New York,2002*

[8] *J. P. Boeuf , Phys. Rev. A, 36,6 (1987)*

[9] *Y. Sakiyama and David B. Graves, Plasma Sources Sci. Technol., 18, 2009*

[10] *Y. Sakiyama, N. Knake, D. Schroder, J. Winter, V. Schulz-von der Gatehn and David B. Graves, Appl. Phys. Lett., 97, 2010*

[11] *Y. Sakiyama and David B. Graves, IEEE Trans. Plasma Sci., 35,5, 2007*

[12] *R Peyrous, P Pignolet & B Held,J. Phys. D: Appl. Phys., 22, 11, 1989*

[13] *Capitelli M.,Ferreira C. M.,Gordiets B. F. and Osipov A. I., Plasma Kinetics in Atmospheric gases, Springer Berlin,2000*

[14] *J. T. Herron & D. S. Green,Plasma Chemistry and Plasma Processing,21,3,2001*

[15] *Doroshenko, V.M.; Kudryavtsev, N.N.; Smetanin, V.V., High Energy Chem., 26,1992*

[16] *D. Stafford and M. J. Kushner, J. Appl. Phys., 96, 5, 2004*

[17] *R. Atkinson and D. L. Baulch and R. A. Cox and R. F. Hampson, Jr. and J. A. Kerr and M. J. Rossi and J. Troe, Journal of Physical and Chemical Reference Data, 26, 6, 1997*

[18] *Y. Sakiyama, D. B. Graves, H-W Chang, T. Shimizu and G. E. Morfill, J. Phys. D: Appl. Phys.,45,2012*

[19] *BOLSIG+, Boltzmann solver, freeware*

[20] *COMSOL Multiphysics ®, partial differential equation solver*

[21] *LXcat, electron scattering database, University of Toulouse*

[22] *Y. B. Golubovskii and V. A. Maiorov and J. Behnke and J. F. Behnke, J. Phys. D: Appl. Phys., 36, 2003*

[23] *I A Kossyi, A Yu Kostinsky, A A Matveyev and V P Silakov, Plasma Sources Sci. Technol., 1, 3, 1992*

[24] *R P Cardoso, T Belmonte, G Henrion, N Sadeghi, J. Phys. D: Appl. Phys., 39, 19, 2006*

[25] *W. S. Kang, H.S. Kim & S. H. Hong,IEEE Trans. Plasma Sci.,38,8,2010*

[26] *M. P. Iannuzzi, J. B. Jeffries & F. Kaufmann,Chem. Phys. Lett.,85,1981*

[27] *R. Dorai & M J Kushner,J. Phys. D: Appl. Phys., 36, 6, 2003*

[28] *L. A. Viehland & E. A. Mason,Atomic Data & Nuclear Data tables, 60, 1995*

[29] *J. Stevefelt,J. M. Pouvesle, A. Bouchoule, The Journal of Chemical Physics, 76, 8, 1982*

[30] *H. Matzing, Advances in Chemical Physics, John Wiley & Sons Inc., 2001*

[31] *Mark J. Kushner, J. Appl. Phys., 74, 11, 1993*

[32] *D. L. Baulch and C. J. Cobos and R. A. Cox and C. Esser and P. Frank and Th. Just and J. A. Kerr and M. J. Pilling and J. Troe and R. W. Walker and J. Warnatz, Journal of Physical and Chemical Reference Data, 21, 3, 1992*

[33] *Boughton J.W. and Kristyan S. and Lin M.C., Chemical Physics, 214, 2, 1997*

[34] *R. Sander Compilation of Henry's Law Constants for Inorganic and Organic Species of Potential Importance in Environmental Chemistry (Version 3) website*

[35] *D X Liu and P Bruggeman and F Iza and M Z Rong and M G Kong Plasma Sources Sci. Technol., 19, 2010*

[36] *M G Kong, G Kroesen, G Morfill, T Nosenko, T Shimizu, J van Dijk and J L Zimmermann New Journal of Physics, 11, 11, 2009*

[37] *G. Fridman, G. Friedman, A. Gutsol, A. B. Shekhtar, V. N. Vasilets, A. Fridman Physics of Plasmas, 5, 6, 2008*

[38] *N Barekzi and M Laroussi J. Phys. D: Appl. Phys., 45, 42, 2012*

[39] *A.Yang and X. Wang and M. Rong and D. Liu and F. Iza and M. G. Kong Physics of Plasmas, 18, 11, 2011*

[40] *Sladek, R. E J and Baede, T.A. and Stoffels, E. IEEE Trans. Plasma Sci., 34, 4, 2006*

[41] *M Yusupov, E C Neyts, U Khalilov, R Snoeckx, A C T van Duin and A Bogaerts New Journal of Physics, 14, 9, 2012*

[42] *S. G. Joshi, M. Cooper, A. Yost, M. Paff, U. K. Ercan, G. Fridman, G. Friedman, A. Fridman and A. D. Brooks Antimicrobial Agents and Chemotherapy, 55, 3, 2011*

[43] *NIST Chemistry WebBook: National Institute of Standards and Technology http://webbook.nist.gov*

[44] *Bruce E. Poling, J. M. Prausnitz, John Paul O'Connell: The properties of gases and liquids, McGraw Hill, 2001*